Astronomy & Astrophysics manuscript no. Cuadrado-HCOOH
November 4, 2016
© ESO 2016

arXiv:1611.01001v1 [astro-ph.GA] 3 Nov 2016

Letter to the Editor

Trans-cis molecular photoswitching in interstellar Space⋆

S. Cuadrado[1], J. R. Goicoechea[1], O. Roncero[2], A. Aguado[3], B. Tercero[1], and J. Cernicharo[1]

[1] Grupo de Astrofísica Molecular. Instituto de Ciencia de Materiales de Madrid (ICMM-CSIC), Sor Juana Ines de la Cruz 3, E-28049 Cantoblanco, Madrid, Spain. e-mail: [s.cuadrado; jr.goicoechea]@icmm.csic.es, jose.cernicharo@csic.es
[2] Instituto de Física Fundamental (IFF-CSIC). Calle Serrano 123, E-28006 Madrid, Spain.
[3] Facultad de Ciencias, Unidad Asociada de Química-Física Aplicada CSIC-UAM, Universidad Autónoma de Madrid, E-28049, Madrid, Spain.

Received October 2016; accepted November 2016

ABSTRACT

As many organic molecules, formic acid (HCOOH) has two conformers (*trans* and *cis*). The energy barrier to internal conversion from *trans* to *cis* is much higher than the thermal energy available in molecular clouds. Thus, only the most stable conformer (*trans*) is expected to exist in detectable amounts. We report the first interstellar detection of *cis*-HCOOH. Its presence in ultraviolet (UV) irradiated gas exclusively (the Orion Bar photodissociation region), with a low *trans*-to-*cis* abundance ratio of 2.8 ± 1.0, supports a photoswitching mechanism: a given conformer absorbs a stellar photon that radiatively excites the molecule to electronic states above the interconversion barrier. Subsequent fluorescent decay leaves the molecule in a different conformer form. This mechanism, which we specifically study with *ab initio* quantum calculations, was not considered in Space before but likely induces structural changes of a variety of interstellar molecules submitted to UV radiation.

Key words. Astrochemistry – Line: identification – ISM: clouds – ISM: molecules – Photon-dominated region (PDR)

1. Introduction

Conformational isomerism refers to isomers (molecules with the same formula but different chemical structure) having the same chemical bonds but different geometrical orientations around a single bond. Such isomers are called conformers. An energy barrier often limits the isomerization. This barrier can be overcome by light. Photoisomerization (or photoswitching) has been studied in ice IR-irradiation experiments (e.g. Maçôas et al. 2004), in biological processes, and, for large polyatomic molecules, also in gas-phase experiments (Ryan & Levy 2001). HCOOH is the simplest organic acid and has two conformers (*trans* and *cis*) depending on the orientation of the hydrogen single bond. The most stable *trans* conformer was the first acid detected in the interstellar medium, ISM (Zuckerman et al. 1971). Gas-phase *trans*-HCOOH shows moderate abundances towards hot cores (Liu et al. 2001) and hot corinos (Cazaux et al. 2003), in cold dark clouds (Cernicharo et al. 2012), and in cometary coma (Bockelée-Morvan et al. 2000). Solid HCOOH is present in interstellar ices (Keane et al. 2001) and in chondritic meteorites (Briscoe & Moore 1993).

The ground-vibrational state of *cis*-HCOOH is $1365 \pm 30\,\mathrm{cm}^{-1}$ higher in energy than the *trans* conformer (Hocking 1976). The energy barrier to internal rotation (the conversion from *trans* to *cis*) is about $4827\,\mathrm{cm}^{-1}$ (Hocking 1976), approximately 7000 K in temperature units. This is much higher than the thermal energy available in molecular clouds (having typical temperatures from about 10 to 300 K). Generalizing this reasoning, only the most stable conformer of a given species would be expected in such clouds. Photoswitching, however, may be a viable mechanism producing the less stable conformers in detectable amounts: a given conformer absorbs a high-energy photon that radiatively excites the molecule to electronic states above the interconversion energy barrier. Subsequent radiative decay to the ground-state would leave the molecule in a different conformer.

In this work we have searched for pure rotational lines of the *trans*- and *cis*-HCOOH conformers in the 3 millimetre spectral band. We observed three prototypical interstellar sources known to display a very rich chemistry and bright molecular line emission: (i) the Orion Bar photodissociation region (PDR): the edge of the Orion cloud irradiated by ultraviolet (UV) photons from nearby massive stars (e.g. Goicoechea et al. 2016), (ii) the Orion hot core: warm gas around massive protostars (e.g. Tercero et al. 2010), and (iii) Barnard 1-b (B1-b): a cold dark cloud (e.g. Cernicharo et al. 2012). The two latter sources are shielded from strong UV radiation fields. We only detect *cis*-HCOOH towards the Orion Bar. This represents the first interstellar detection of the conformer.

2. Source selection and observations

Because of its nearly edge-on orientation, the Orion Bar PDR is a template source to study the molecular content as the far-UV radiation field (FUV; stellar photons with energies below 13.6 eV, or wavelengths (λ) longer than 911 Å, the hydrogen atom ionisation threshold) is attenuated from the cloud edge to the interior (Hollenbach & Tielens 1999). The impinging FUV radiation field at the edge of the Bar is about 4×10^4 times the mean interstellar radiation field (e.g. Goicoechea et al. 2016, and references therein). We observed three positions of the Bar characterized by a decreasing FUV photon flux.

⋆ This paper makes use of observations obtained with the IRAM-30 m telescope. IRAM is supported by INSU/CNRS (France), MPG (Germany), and IGN (Spain).

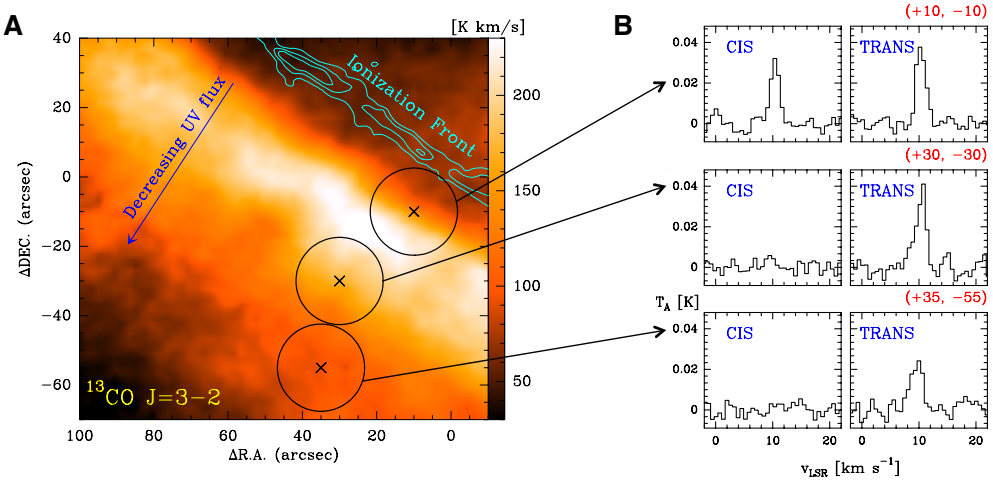

Fig. 1. Detection of *cis*-HCOOH towards the FUV-illuminated edge of the Orion Bar. *Left*: ^{13}CO $J = 3 \rightarrow 2$ integrated emission image with a HPBW of 8″ obtained with the IRAM-30 m telescope (Cuadrado et al. in prep.). The cyan contour marks the position of neutral cloud boundary traced by the O I 1.317 μm fluorescent line emission (in contours from 3 to 7 by 2×10^{-4} erg s^{-1} cm^{-2} sr^{-1}; Walmsley et al. 2000). *Right*: *Cis*- and *trans*-HCOOH stacked spectra towards the observed positions.

We have used the IRAM-30 m telescope (Pico Veleta, Spain) and the 90 GHz EMIR receiver. We employed the Fast Fourier Transform Spectrometer (FFTS) backend at 200 kHz spectral resolution (0.7 km s^{-1} at 90 GHz). Observations towards the Orion Bar are part of a complete millimetre (mm) line survey (80 − 360 GHz, Cuadrado et al. 2015). They include specific deep searches for HCOOH lines in the 3 mm band towards three different positions located at a distance of 14″, 40″, and 65″ from the ionisation front (Fig. 1A). Their offset coordinates with respect to the $\alpha_{2000} = 05^h\,35^m\,20.1^s$, $\delta_{2000} = -05°25'07.0''$ position at the ionisation front are (+10″, -10″), (+30″, -30″'), and (+35″, -55″). The observing procedure was position switching with a reference position at (−600″, 0″) to avoid the extended emission from the Orion molecular cloud. The half power beam width (HPBW) at 3 mm ranges from ∼30.8″ to 21.0″. We reduced and analysed the data using the GILDAS software as described in Cuadrado et al. (2015). The antenna temperature, T_A^*, was converted to the main beam temperature, T_{MB}, using $T_{MB} = T_A^*/\eta_{MB}$, where η_{MB} is the antenna efficiency ($\eta_{MB} = 0.87 - 0.82$ at 3 mm). The rms noise obtained after 5 h integration is ∼1 − 5 mK per resolution channel.

We also searched for HCOOH in regions shielded from strong FUV radiation fields (see Appendix E). We selected two chemically rich sources for which we have also carried out deep mm-line surveys with the IRAM-30m telescope: towards the hot core in Orion BN/KL (Tercero et al. 2010) and towards the quiescent dark cloud Barnard 1-b (B1-b; Cernicharo et al. 2012).

3. Results

3.1. Line identification

We specifically computed the *cis*-HCOOH rotational lines frequencies by fitting the available laboratory data (Winnewisser et al. 2002) with our own spectroscopic code, MADEX (Cernicharo 2012). The standard deviation of the fit is 60 kHz. For the *trans* conformer, higher frequency laboratory data (Cazzoli et al. 2010) were also used in a separate fit. The standard deviation of the fit for *trans*-HCOOH is 42 kHz. These deviations are smaller than the frequency resolution of the spectrometer we used to carry out the astronomical observations. Formic acid is a near prolate symmetric molecule with rotational levels distributed in different K_a rotational ladders (K_a = 0, 1, 2...). Both *a*- and *b*-components of its electric dipole moment μ exist (Winnewisser et al. 2002). The dipole moments of the *cis* conformer (μ_a = 2.650 D and μ_b = 2.710 D, Hocking 1976) are stronger than those of the *trans* conformer (μ_a = 1.421 D and μ_b = 0.210 D, Kuze et al. 1982).

In total, we identify 12 rotational lines of *cis*-HCOOH and 10 of *trans*-HCOOH above 3σ towards the FUV-illuminated edge of the Orion Bar, (+10″, -10″) position. The detected lines from the *cis*- and *trans*-HCOOH are shown in Figs. 2 and D.1, respectively. Lines attributed to HCOOH show a Gaussian line profile centred at the systemic velocity of the Orion Bar (10.4 ± 0.3 km s^{-1}). Lines are narrow, with linewidths of 1.9 ± 0.3 km s^{-1}. The large number of detected lines, and the fact that none of the lines correspond to transitions of abundant molecules known to be present in the Bar or in spectroscopic line catalogues, represents a robust detection of the *cis* conformer. The observational parameters and Gaussian fit results are tabulated in Tables F.1 and F.2 for the *cis* and *trans* conformer, respectively.

3.2. Line stacking analysis

Complex organic molecules have relatively low abundances in FUV-irradiated interstellar gas (Guzmán et al. 2014). Indeed, detected *trans*-HCOOH lines are faint. To improve the statistical significance of our search towards the positions inside the Bar, we performed a "line stacking" analysis. For each observed position, we added spectra at the expected frequency of several HCOOH lines that could be present within the noise level (sharing similar rotational level energies and Einstein coefficients). The spectra in frequency scale were first converted to local standard of rest (LSR) velocity scale and resampled to the same velocity channel resolution before stacking. We repeated this procedure for *trans*-HCOOH lines. This method allows us to search for any weak line signal from the two conformers that could not be detected individually.

Figure 1B shows a comparison of the stacking results for *cis* and *trans*-HCOOH lines towards the three target positions in the Bar. Although we detect *trans*-HCOOH in all positions, emis-

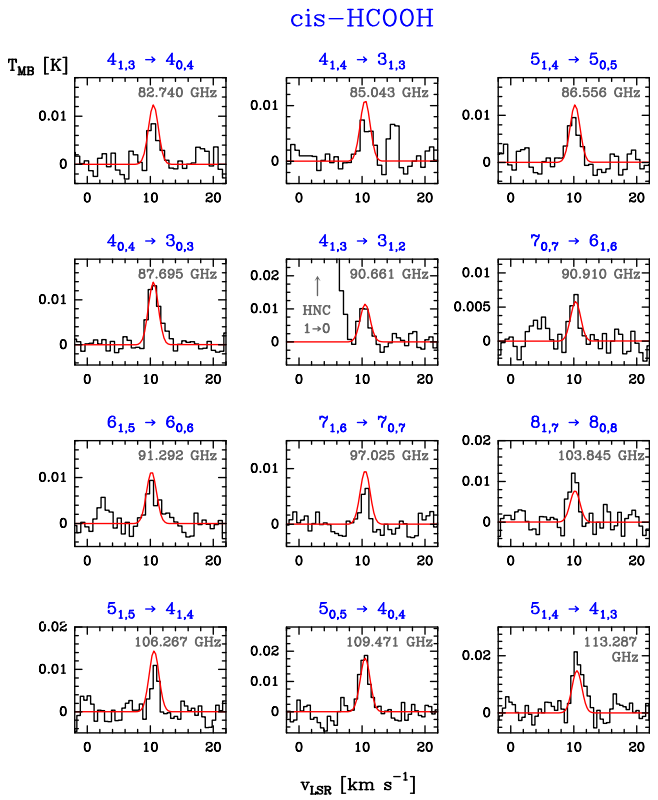

Fig. 2. Detected *cis*-HCOOH rotational lines towards the Orion Bar, (+10″, -10″) position. The ordinate refers to the intensity scale in main beam temperature units, and the abscissa to the LSR velocity. Line frequencies (in GHz) are indicated at the top-right of each panel together with the rotational quantum numbers (in blue). The red curve shows an excitation model that reproduces the observations.

sion from the *cis* conformer is only detected towards the position located closer to the cloud edge, (+10″, -10″). They demonstrate that *cis*-HCOOH is detected close the FUV-illuminated edge of the Bar, but the emission disappears towards the more shielded cloud interior.

A similar stacking analysis was carried out for the Orion hot core and B1-b spectra. Although we detect several *trans*-HCOOH lines, the *cis* conformer was not detected towards the hot core and the cold dark cloud (see Appendix E).

3.3. Trans-to-cis abundance ratios

Given the number of HCOOH lines detected towards the Bar, we can determine the column density and rotational temperatures of both conformers accurately (see Appendix D). In particular, we infer a low *trans*-to-*cis* abundance ratio of 2.8 ± 1.0. The non-detection of *cis*-HCOOH towards the Orion hot core and B1-b (see Appendix E) provides much higher *trans*-to-*cis* limits (>100 and >60, respectively). This suggests that the presence of *cis*-HCOOH in the Orion Bar PDR is related to the strong FUV field permeating the region.

4. Photoisomerization rates and discussion

Photolysis of HCOOH has been widely studied, both experimentally (Sugarman 1943; Ioannoni et al. 1990; Brouard & Wang 1992; Su et al. 2000) and theoretically (Beaty-Travis et al. 2002; He & Fang 2003; Maeda et al. 2015). Dissociation of HCOOH takes place after absorption of FUV photons with energies greater than ∼5 eV (λ < 2500 Å). Recently, Maeda et al. (2015) determined that this dissociation threshold coincides with the crossing of the S_0 and T_1 electronic states of the molecule. The specific products of the photofragmentation process (of the different photodissociation channels) depend on the specific energy of the FUV photons and on the initial HCOOH conformer. Interestingly, absorption of lower energy photons does not dissociate the molecule but induces fluorescent emission. In particular, HCOOH fluorescence from the S_1 excited electronic state has been observed in laser-induced experiments performed in the λ = 2500 − 2700 Å range (Ioannoni et al. 1990; Brouard & Wang 1992). These studies indicate that the geometrical configuration of the two hydrogen atoms is different in the S_0 and S_1 states. The fluorescence mechanism from the S_1 state is a likely route for the *trans* → *cis* isomerization. In addition, the isomerization barrier from the S_1 state (∼1400 cm^{-1}) is much lower than from the ground.

In order to quantify the role of the photoswitching mechanism, we carried out *ab initio* quantum calculations and determined the HCOOH potential energy surfaces of the S_0 and S_1 electronic states as a function of the two most relevant degrees of freedom, ϕ_1 the torsional angle of OH and ϕ_2, the torsional angle of CH (see Appendix A and Fig. A.1). With this calculation we can compute the position of the photon absorptions leading to fluorescence (those in the approximate λ = 2300 − 2800 Å range), and the probabilities to fluoresce from one conformer to the other (the *trans*-to-*cis* and *cis*-to-*trans* photoswitching cross-sections and probabilities, see Fig. 3).

With a knowledge of $N_{\rm ph}(\lambda)$, the FUV photon flux in units of photon cm^{-2} s^{-1} Å^{-1}, we can calculate the number of *trans*-to-*cis* and *cis*-to-*trans* photoisomerizations per second ($\xi_{\rm tc}$ and $\xi_{\rm ct}$, respectively. See Appendix B). In the absence of any other mechanism destroying HCOOH, the $\xi_{\rm ct}/\xi_{\rm tc}$ ratio provides the *trans*-to-*cis* abundance ratio in equilibrium. The time needed to reach the equilibrium ratio is then $(\xi_{\rm tc} + \xi_{\rm ct})^{-1}$. $N_{\rm ph}(\lambda)$, and thus $\xi_{\rm tc}$ and $\xi_{\rm ct}$, depend on the FUV radiation sources (type of star) and on the cloud position. Describing the cloud depth position in terms of the visual extinction into the cloud ($A_{\rm V}$), one magnitude of extinction is equivalent to a column density of about 10^{21} H_2 molecules per cm^{-2} in the line-of-sight.

In general (for a flat, wavelength-independent FUV radiation field), HCOOH photodissociation will always dominate over fluorescence (photodissociation cross-sections are larger and the relevant photons can be absorbed over a broader energy range, $E > 5$ eV). The strength and shape of the interstellar FUV radiation field, however, is a strong function of $A_{\rm V}$ and is very sensitive to the dust and gas absorption properties. Because of the wavelength-dependence of the FUV-absorption process, $N_{\rm ph}(\lambda)$ drastically changes as one moves from the cloud edge to the shielded interior. In particular, the number of low-energy FUV photons (e.g. below 5 eV) relative to the high-energy photons (e.g. those above 11 eV dissociating molecules such as CO and ionising atoms such as carbon) increases with $A_{\rm V}$. In this work we used a FUV radiative transfer and thermo-chemical model (Le Petit et al. 2006; Goicoechea & Le Bourlot 2007) to estimate $N_{\rm ph}(\lambda)$ at different positions of the Orion Bar. The well-known "2175 Å bump" of the dust extinction curve (absorption of λ = 1700 − 2500 Å photons by PAHs and small carbonaceous grains, Cardelli et al. 1989; Joblin et al. 1992) greatly reduces the number of HCOOH dissociating photons relative to those producing HCOOH fluorescence (Fig. 3, bottom panel). The resulting FUV radiation spectrum, $N_{\rm ph}(\lambda)$, at different $A_{\rm V}$ is used

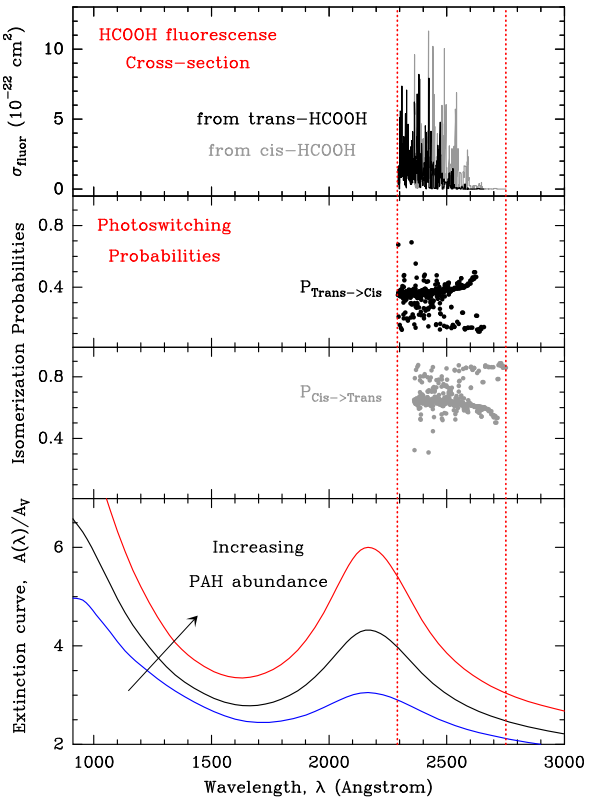

Fig. 3. *Ab initio* absorption cross-sections and photoisomerization probabilities computed in this work. *Top panel*: *trans*- and *cis*-HCOOH absorption cross-sections for photons with $E < 5$ eV (those leading to fluorescence). *Middle panels*: normalized probabilities of bound-bound decays producing isomerization (*trans* → *cis* and *cis* → *trans*). *Bottom panel*: standard interstellar dust extinction curve (blue). Black and red curves show the effect of an increased PAH abundance.

to calculate ξ_{tc} and ξ_{ct} (Table B.1). We determine that at a cloud depth of about $A_V = 2 - 3$ mag, and if the number of HCOOH dissociating photons is small compared to the number of photons producing photoisomerization (i.e. most photons with $E > 5$ eV have been absorbed), the *cis* conformer should be detectable with a *trans*-to-*cis* abundance ratio of about 3.5 − 4.1. These values are remarkably close to the *trans*-to-*cis* ratio inferred from our observations of the Bar.

Closer to the irradiated cloud edge ($A_V = 0 - 2$ mag), photodissociation destroys the molecule much faster than the time needed for the *trans*-to-*cis* isomerization. On the other hand, too deep inside the cloud, the flux of $E > 5$ eV photons decreases to values for which the isomerization equilibrium would take an unrealistic amount of time (>10^6 years for $A_V = 5$ mag). Therefore, our detection of *cis*-HCOOH in irradiated cloud layers where CO becomes the dominant carbon carrier (a signature of decreasing flux of high-energy FUV photons) agrees with the photoswitching scenario.

For standard grain properties and neglecting HCOOH photodissociation, we calculate that the time needed to achieve a low *trans*-to-*cis* abundance ratio and make *cis*-HCOOH detectable at $A_V = 2 - 3$ mag is $10^4 - 10^5$ years (see Table B.1). This is reasonably fast, and shorter than the cloud lifetime. In practice, it is not straightforward to quantify the exact contribution of HCOOH photodissociation and photoisomerization at different cloud positions. The above time-scales require that the flux of $E > 5$ eV dissociating photons is small compared to those producing fluorescence. This depends on the specific dust absorption properties, that sharply change with A_V as dust populations evolve (Draine 2003), on the strength and width of the 2175 Å extinction bump, and on the role of molecular electronic transitions blanketing the FUV spectrum. The similar *trans*-HCOOH line intensities observed towards the three positions of the Bar (Fig. 1) suggest that even if the HCOOH photodestruction rate increases at the irradiated cloud edge, the HCOOH formation rate (from gas-phase reactions or desorbing directly from grain surfaces, Garrod et al. 2008) must increase as well. The inferred HCOOH abundances are not particularly high, $(0.6 - 3.0) \times 10^{-10}$ with respect to H. Hence, modest HCOOH photodestruction and formation rates are compatible with the photoswitching mechanism occurring in realistic times.

Although the observed abundances of *trans*- and *cis*-HCOOH in the Orion Bar are compatible with gas-phase photoisomerization, we note that photoswitching may also occur on the surface of grains covered by HCOOH ices. In a similar way, solid HCOOH (mostly *trans*) can absorb FUV photons that switch the molecule to the *cis* form before being desorbed. Once in the gas, both conformers will continue their photoisomerization following absorption of $\lambda \gtrsim 2500$ Å photons. Laboratory experiments are needed to quantify the mechanisms leading to HCOOH ice photoswitching by FUV photon absorption.

Searching for further support to the FUV photoswitching scenario, we qualitatively explored two other possibilities for the *trans*-to-*cis* conversion. First, the isomerization of solid HCOOH after IR irradiation of icy grain surfaces (as observed in the laboratory, Maçôas et al. 2004; Olbert-Majkut et al. 2008) and subsequent desorption to the gas-phase. Second, the gas-phase isomerization by collisions of HCOOH with energetic electrons (~0.5 eV). We concluded that if these were the dominant isomerization mechanisms, emission lines from *cis*-HCOOH would have been detected in other interstellar sources (see Appendix C).

Isomerization by absorption of UV photons was not considered as a possible mechanism to induce structural changes of molecules in interstellar gas. The detection of *cis*-HCOOH towards the Orion Bar opens new avenues to detect a variety of less stable conformers in Space. This can have broad implications in astrochemistry and astrobiology.

Acknowledgements. We thank N. Marcelino for helping with the observations of B1-b. We thank the ERC for support under grant ERC-2013-Syg-610256-NANOCOSMOS. We also thank Spanish MINECO for funding support under grants AYA2012-32032 and FIS2014-52172-C2, and from the CONSOLIDER-Ingenio program "ASTROMOL" CSD 2009-00038. IRAM is supported by INSU/CNRS (France), MPG (Germany), and IGN (Spain).

References

Beaty-Travis, L. M., Moule, D. C., Lim, E. C., & Judge, R. H. 2002, J. Chem. Phys., 117, 4831
Blake, G. A., Sutton, E. C., Masson, C. R., & Phillips, T. G. 1987, ApJ, 315, 621
Bockelée-Morvan, D., Lis, D. C., Wink, J. E., et al. 2000, A&A, 353, 1101
Briscoe, J. F. & Moore, C. B. 1993, Meteoritics, 28, 330
Brouard, M. & Wang, J.-X. 1992, J. Chem. Soc., Faraday Trans., 88, 3511
Cardelli, J. A., Clayton, G. C., & Mathis, J. S. 1989, ApJ, 345, 245
Cazaux, S., Tielens, A. G. G. M., Ceccarelli, C., et al. 2003, ApJ, 593, L51
Cazzoli, G., Puzzarini, C., Stopkowicz, S., & Gauss, J. 2010, A&A, 520, A64
Cernicharo, J. 2012, in EAS Publications Series, Vol. 58, 251–261
Cernicharo, J., Kisiel, Z., Tercero, B., et al. 2016, A&A, 587, L4
Cernicharo, J., Marcelino, N., Roueff, E., et al. 2012, ApJ, 759, L43
Cuadrado, S., Goicoechea, J. R., Pilleri, P., et al. 2015, A&A, 575, A82
Draine, B. T. 1978, ApJS, 36, 595
Draine, B. T. 2003, ARA&A, 41, 241
Garrod, R. T., Widicus Weaver, S. L., & Herbst, E. 2008, ApJ, 682, 283
Gerin, M., Pety, J., Fuente, A., et al. 2015, A&A, 577, L2

Goicoechea, J. R. & Le Bourlot, J. 2007, A&A, 467, 1
Goicoechea, J. R., Pety, J., Cuadrado, S., et al. 2016, Nature, 537, 207
Goldsmith, P. F. & Langer, W. D. 1999, ApJ, 517, 209
Guzmán, V. V., Pety, J., Gratier, P., et al. 2014, Faraday Discussions, 168, 103
He, H.-Y. & Fang, W.-H. 2003, Journal of the American Chemical Society, 125, 16139
Hocking, W. H. 1976, Zeitschrift Naturforschung Teil A, 31, 1113
Hollenbach, D. J. & Tielens, A. G. G. M. 1999, Reviews of Modern Physics, 71, 173
Ioannoni, F., Moule, D. C., & Clouthier, D. J. 1990, The Journal of Physical Chemistry, 94, 2290
Joblin, C., Leger, A., & Martin, P. 1992, ApJ, 393, L79
Jørgensen, J. K., Harvey, P. M., Evans, II, N. J., et al. 2006, ApJ, 645, 1246
Keane, J. V., Tielens, A. G. G. M., Boogert, A. C. A., Schutte, W. A., & Whittet, D. C. B. 2001, A&A, 376, 254
Kuze, H., Kuga, T., & Shimizu, T. 1982, Journal of Molecular Spectroscopy, 93, 248
Le Petit, F., Nehmé, C., Le Bourlot, J., & Roueff, E. 2006, ApJS, 164, 506
Li, A. & Draine, B. T. 2001, ApJ, 554, 778
Liu, S.-Y., Mehringer, D. M., & Snyder, L. E. 2001, ApJ, 552, 654
Maçôas, E. M. S., Khriachtchev, L., Pettersson, M., Fausto, R., & Räsänen, M. 2004, J. Chem. Phys., 121, 1331
Maeda, S., Taketsugu, T., & Morokuma, K. 2012, The Journal of Physical Chemistry Letters, 3, 1900
Maeda, S., Taketsugu, T., Ohno, K., & Morokuma, K. 2015, Journal of the American Chemical Society, 137, 3433
Marcelino, N. 2007, PhD thesis, Universidad de Granada, Spain
Öberg, K. I., Bottinelli, S., Jørgensen, J. K., & van Dishoeck, E. F. 2010, ApJ, 716, 825
Olbert-Majkut, A., Ahokas, J., Lundell, J., & Pettersson, M. 2008, J. Chem. Phys., 129, 041101
Ryan, W. L. & Levy, D. H. 2001, Journal of the American Chemical Society, 123, 961
Su, H., He, Y., Kong, F., Fang, W., & Liu, R. 2000, J. Chem. Phys., 113, 1891
Sugarman, B. 1943, Proceedings of the Physical Society, 55, 429
Tercero, B., Cernicharo, J., Pardo, J. R., & Goicoechea, J. R. 2010, A&A, 517, A96
van Dishoeck, E. F. & Black, J. H. 1982, ApJ, 258, 533
Walmsley, C. M., Natta, A., Oliva, E., & Testi, L. 2000, A&A, 364, 301
Werner, H.-J., Knowles, P. J., Knizia, G., Manby, F. R., & Schtz, M. 2012, Wiley Interdisciplinary Reviews: Computational Molecular Science, 2, 242
Winnewisser, M., Winnewisser, B. P., Stein, M., et al. 2002, Journal of Molecular Spectroscopy, 216, 259
Zuckerman, B., Ball, J. A., & Gottlieb, C. A. 1971, ApJ, 163, L41

Appendix A: *Ab initio* estimation of fluorescence cross-sections and photoisomerization probabilities

In this appendix, we demonstrate that the detected *cis*-HCOOH towards the Orion Bar can be produced by a gas-phase photoswitching mechanism. To estimate the FUV photon absorption cross-sections and probabilities of the *trans-cis* photoisomerization process, we start calculating the potential energy surfaces of the HCOOH S_0 and S_1 electronic states as a function of the two most relevant degrees of freedom, the torsional angle of OH (ϕ_1), and the torsional angle of CH (ϕ_2) (see Fig. A.1).

We performed ic-MRCI-F12 *ab initio* calculations using the MOLPRO suite of programs[1] with the VDZ-F12 basis set. The obtained results agree with the stationary points previously reported by Maeda et al. (2012, 2015). The molecular orbitals and reference configurations were determined with a CASSCF calculation using 16 active orbitals. The optimized equilibrium geometries in the S_0 and S_1 electronic states are in agreement with previous results, corresponding to planar and bent *trans*-HCOOH conformers, respectively. They are listed in Table A.1.

[1] MOLPRO (Werner et al. 2012), version 2012, is a package of *ab initio* programs for advanced molecular electronic structure calculations, designed and maintained by H.-J. Werner and P. J. Knowles, and with contributions from many other authors (see http://www.molpro.net).

For *trans*-HCOOH, the normal modes in the S_0 state have the following frequencies: 628.59, 662.86, 1040.64, 1117.90, 1316.0, 1416.22, 1792.32, 3083.01, and 3749.88 cm^{-1}. The two lowest frequencies correspond to the torsional angles of the OH and CH bonds, respectively.

For the two lower singlet states, S_0 and S_1, we calculate a two-dimensional grid composed of 37 equally spaced points for ϕ_1 and ϕ_2, fixing the rest of coordinates to the corresponding values listed in Table A.1. These points are interpolated using a two-dimension splines method to get the potential energy surfaces, S_0 and S_1, at any desired geometry, including the two conformers.

The potential energy surface of the S_0 electronic state presents two minima for $\phi_2 = 0°$, one at $\phi_1 = 0°$ or 360° (*trans*), and a second at $\phi_1 = 180°$ (*cis*). As illustrated in Fig. A.1, both minima correspond to a planar geometry. The potential for the S_1 excited state presents two equivalent wells for the *trans*-conformer ($\phi_1 = 300°$, $\phi_2 = 120°$ or $\phi_1 = 60°$, $\phi_2 = 240°$). Therefore, the minimum geometrical configuration in the S_1 excited state is no longer planar. The *cis* conformer minimum transforms into a shoulder of the potential. This is shown in the one-dimensional cut shown in Fig. A.1 for the case of $\phi_2 = 120°$. In this case, the potential energy surface as a function of ϕ_1 is rather flat, while it shows a double-well structure as a function of ϕ_2, corresponding to geometries above and below the molecular plane.

Table A.1. Optimized geometries for *trans*-HCOOH in the ground (S_0) and excited electronic state (S_1). Distances are in Angstrom and angles in degree units.

Geometry of *trans*-HCOOH	S_0 ground-state (geom-S_0)	S_1 excited-state (geom-S_1)
$R(CO_1)$	1.1987	1.3683
$R(CO_2)$	1.3600	1.3840
$\theta(O_1CO_2)$	122.38	111.17
$R(CH_1)$	1.1008	1.0751
$\theta(O_1CH_1)$	124.01	113.06
$R(OH_1)$	0.9663	0.9661
$\theta(CO_2H_2)$	108.72	107.51
$\phi_1(H_2O_2CO_1)$	0.00	55.32
$\phi_2(H_1CO_1O_2)$	180.00	232.28

We solved the two-dimension Shrödinger equation for ϕ_1 and ϕ_2 and obtained the vibrational eigenfunctions. The first six vibrational levels of the S_0 electronic state correspond to the *trans* conformer, the seventh energy level corresponds to the ground-vibrational state of *cis*-HCOOH. In the S_1 excited electronic state, the presence of a double well as a function of ϕ_2 implies that two degenerate vibrational states appear. The two well depths are different in geom-S_0 and geom-S_1 which means that their nodal structure significantly changes.

In a second step, we calculate the transition dipole moments for the two-dimensional grids of geom-S_0 and geom-S_1, and determine the transitions between the S_0 state and the S_1 state. We derive the absorption spectra starting from both *trans*-HCOOH ($\nu = 0$) and *cis*-HCOOH ($\nu = 7$) in the S_0 electronic ground-state, to the first 200 vibrational levels of the S_1

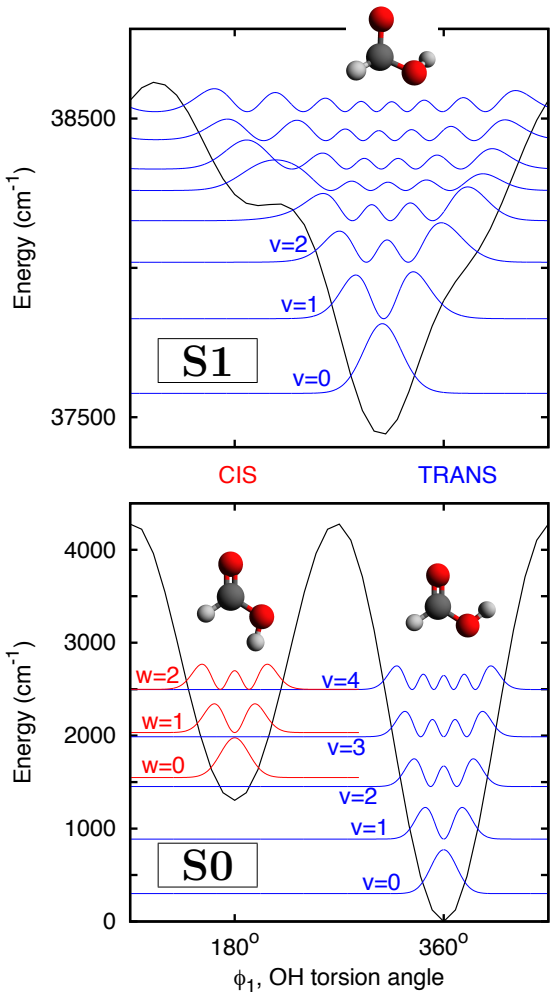

Fig. A.1. One-dimensional potential energy surfaces of HCOOH as function of the OH torsional angle ϕ_1. *Bottom panel*: ground S_0 electronic state. *Top panel*: excited S_1 state. One-dimensional cuts were obtained from the two-dimensional grid (see text) by setting $\phi_2 = 180°$ and $\phi_2 = 300°$ for S_0 and S_1, respectively. We also show the vibrational-wave functions obtained from a one-dimensional model. The different geometrical structures of the HCOOH molecule in each energy minimum are shown.

excited-state. The use of different geometries in the two electronic states allows us to approximately reproduce the experimental frequencies (Beaty-Travis et al. 2002). The absorption spectrum is obtained using the transition dipole moments obtained for geom-S_0.

The calculated radiative lifetimes of the different vibrational levels of the S_1 electronic excited-state vary from 75×10^{-6} s to 375×10^{-6} s, but each level has a different probability to decay towards the *trans* of *cis* well of the S_0 ground electronic state. We explicitly determine the probability to fluoresce into each conformer by calculating:

$$P_{cis\,(\nu)} = \sum_{\nu', cis} \left| < f_{\nu'}^{S_0} \,|\, d \,|\, f_{\nu}^{S_1} > \right|^2 \qquad \text{(A.1)}$$

and

$$P_{trans\,(\nu)} = \sum_{\nu', trans} \left| < f_{\nu'}^{S_0} \,|\, d \,|\, f_{\nu}^{S_1} > \right|^2 \qquad \text{(A.2)}$$

where we separate the contributions of the ν' levels corresponding to the *trans* or *cis* conformers and normalize the sum to 1. We then normalize the above values and compute $P_{cis}(\nu)/(P_{cis}(\nu)+P_{trans}(\nu))$ and $P_{trans}(\nu)/(P_{cis}(\nu)+P_{trans}(\nu))$ for ν levels corresponding to absorption energies below about 40000 cm^{-1} ($E < 5$ eV), approximately the energy for which the dominant photodissociation channel opens and fluorescence starts to become negligible.

In summary, with these *ab initio* calculations we estimate the *cis*- and *trans*-HCOOH cross-sections σ_{λ_i} for absorption of photons with energies lower than about 40000 cm^{-1} (those producing fluorescense). These absorptions radiatively excite the molecule to the S_1 electronic excited-state. We explicitly compute the σ_{λ_i} values for each photon energy as well as the probabilites to fluoresce back to a specific *cis* or *trans* state (i.e. we determine the normalized probabilities of the different *trans* → *cis*, *trans* → *trans*, *cis* → *cis*, *cis* → *trans* bound-bound transitions). The $\sigma_{\lambda_i}(trans)$ and $\sigma_{\lambda_i}(cis)$ cross-sections and the $P_{trans\to cis}$ and $P_{cis\to trans}$ probabilities are plotted in Fig. 3.

Appendix B: Estimation of the photoisomerization rate in the Orion Bar

The number of photoisomerizations per second depends on the flux of FUV photons with energies below 5 eV. The *trans*-to-*cis* and *cis*-to-*trans* photoisomerization rates (ξ_{tc} and ξ_{ct}) are derived from the discrete sums:

$$\xi_{tc} = \sum_{\lambda_i} N_{ph,\,\lambda_i} \cdot \sigma_{\lambda_i}(trans) \cdot P_{t\to c} \qquad \text{(B.1)}$$

and

$$\xi_{ct} = \sum_{\lambda_i} N_{ph,\,\lambda_i} \cdot \sigma_{\lambda_i}(cis) \cdot P_{c\to t} \qquad \text{(B.2)}$$

where σ_{λ_i} is the absorption cross-section from a given conformer (in cm^2 $photon^{-1}$) and P is the probability to fluoresce from one isomer to the other. Both quantities are determined from our *ab initio* calculations (previous section). $N_{ph,\,\lambda_i}$ (photon cm^{-2} s^{-1}) is the flux of photons at each wavelength producing absorption.

In order to estimate the most realistic ξ_{tc} and ξ_{ct} rates for the FUV-irradiation conditions in the Orion Bar, we used the Meudon PDR code (Le Petit et al. 2006) and calculate $N_{ph}(\lambda)$ at different cloud depth A_V values. Following our previous studies of the Bar (Cuadrado et al. 2015; Goicoechea et al. 2016) we run a model of an isobaric PDR ($P_{th}/k = 10^8$ K cm^{-3}) illuminated by $\chi = 4 \times 10^4$ times the mean interstellar radiation field (Draine 1978). For photons in the $\lambda = 2000 - 3000$ Å range, we adopt $N_{ph}(\lambda) = 4 \times 10^4 \times 732 \times \lambda^{0.7}$ photon cm^{-2} s^{-1} $Å^{-1}$ at the PDR edge ($A_V = 0$) (van Dishoeck & Black 1982). We use a constant dust composition and size distribution that reproduces standard interstellar extinction curve (Cardelli et al. 1989).

Table B.1 shows the resulting photoisomerization rates at different cloud depths, the expected *trans*-to-*cis* HCOOH abundance ratio at equilibrium, and the time needed to reach the equilibrium ratios (neglecting photodissociation).

The use of constant dust grain properties through the PDR is likely the most important simplification for the calculation of the photoisomerization rates ξ_{tc} and ξ_{ct}. Grain populations are known to evolve in molecular clouds, especially in PDRs where the sharp attenuation of a strong FUV field results in a stratification of the dust and PAH properties with A_V (Draine 2003). Therefore, although the varying optical properties of grains are difficult to quantify and include in PDR models, they likely play

Table B.1. Photoisomerization rates for the irradiation conditions in the Orion Bar.

Cloud depth A_V [mag]	N_{ph} (2300 – 2800 Å) [photons cm^{-2} s^{-1}]	ξ_{tc} [s^{-1}]	ξ_{ct} [s^{-1}]	*trans*/*cis*-HCOOH ratio at equilibrium	Time [years]
0	1.96×10^{12}	5.45×10^{-11}	1.27×10^{-10}	2.3	1.7×10^{2}
1	1.80×10^{11}	3.41×10^{-12}	9.89×10^{-12}	2.9	2.4×10^{3}
2	2.84×10^{10}	3.79×10^{-13}	1.31×10^{-12}	3.5	1.9×10^{4}
3	4.93×10^{9}	4.62×10^{-14}	1.87×10^{-13}	4.1	1.3×10^{5}
5	1.69×10^{8}	7.83×10^{-16}	4.29×10^{-15}	5.5	6.2×10^{6}

a role on how FUV photons of different energies are differentially absorbed as a function of A_V (Goicoechea & Le Bourlot 2007). For the particular case of HCOOH, the strength and width of the 2175 Å extinction bump (Cardelli et al. 1989) naturally divides the range of photons producing HCOOH photodissociation (those with $E > 5$ eV) from those producing fluorescence ($E < 5$ eV). The extinction bump has been related with the absorption of FUV photons by PAH mixtures and small carbonaceous grains (Joblin et al. 1992; Draine 2003). Although it is not known how the bump evolves with A_V, it clearly determines how the lower-energy FUV photons are absorbed. In Fig. 3 (bottom panel) we show different extinction curves for different PAH abundances (Goicoechea & Le Bourlot 2007). Optical properties are taken from Li & Draine (2001) and references therein. In addition, and as in most PDR models, our predicted FUV spectrum does not include the absorption produced by hundreds of molecular electronic transitions blanketing the FUV spectrum (other than H_2 and CO lines). All together, our assumption that the detected *cis*-HCOOH arises from PDR layers in which the flux of photons with $\lambda > 2500$ Å dominates over the higher-energy photodissociating photons is very plausible.

Appendix C: Alternative mechanisms for *trans*-to-*cis* isomerization in the ISM

Searching for further support to the photoswitching scenario, we qualitatively explored other possibilities that may apply in interstellar conditions. In the laboratory, *trans*-to-*cis* isomerization has been observed in molecular ices irradiated by near-IR photons (Maçôas et al. 2004; Olbert-Majkut et al. 2008). Hence, isomerization of solid HCOOH and subsequent desorption to the gas-phase might also be responsible of the *cis*-HCOOH enhancement. However, owing to the short lifetime of the *cis* conformer observed in ices (a few minutes if the irradiation is stopped, Maçôas et al. 2004), a very strong flux of IR photons would be needed to maintain significant abundances of solid *cis*-HCOOH. In addition, near-IR photons penetrate molecular clouds much deeper than FUV photons, and one would have expected to detect *cis*-HCOOH in all positions of the Bar, and towards the Orion hot core, a region irradiated by intense IR fields. Alternatively, the *trans*-to-*cis* isomerization might be triggered by collisions with electrons. Electrons are relatively abundant in FUV-irradiated environments (with ionisation fractions up to about $n_e/n_H \approx 10^{-4}$) compared to shielded cloud interiors ($n_e/n_H \approx 10^{-9}$). Simple calculations show that electrons with energies of about 0.5 eV would be needed to overcome the energy barrier to HCOOH isomerization, and to produce a *trans*-to-*cis* abundance ratio of about 3. Such suprathermal electrons could be provided by the photoionisation of low ionisation potential atoms (C, S, Si...), but their abundance sharply decrease with A_V (Hollenbach & Tielens 1999). We estimate that at a cloud depth of $A_V = 2$ mag, HCOOH collisional isomerization, if effective, could compete with photoswitching only if the elastic collisional rate coefficients were very high, of the order of $>10^{-6}$ cm^3 s^{-1} for a typical electron density of $n_e < 1$ cm^{-3} in PDRs. However, the detection of *trans*-HCOOH, but not *cis*-HCOOH, towards other PDRs such as the Horsehead (Guzmán et al. 2014), with similar electron densities but much lower FUV photon flux (>100 times less than the Bar), supports a photoswitching mechanism in the Orion Bar (i.e. high ξ_{tc} and ξ_{ct} rates), but makes it too slow for the Horsehead and other low FUV-flux sources. Either way, we encourage laboratory and theoretical studies of the possible role of electron collisions, as well as of a more detailed investigation of the HCOOH, and other species, photoswitching mechanism.

Appendix D: Rotational diagrams and column density calculation

Owing to the large number of detected HCOOH lines, we calculated rotational temperatures (T_{rot}) and column densities (N) from rotational population diagrams. The standard relation for the rotational diagram (Goldsmith & Langer 1999) is:

$$\ln \frac{N_u}{g_u} = \ln N - \ln Q_{T_{rot}} - \frac{E_u}{k T_{rot}}, \quad \text{(D.1)}$$

with N_u/g_u given by

$$\frac{N_u}{g_u} = \frac{8\pi k}{h c^3} \cdot \frac{\nu_{ul}^2}{A_{ul}\, g_u} \cdot \eta_{bf}^{-1} \cdot \int T_{MB} dv \quad [cm^{-2}], \quad \text{(D.2)}$$

In the above relation, N_u is the column density of the upper level in the optically thin limit [cm^{-2}], N is the total column density [cm^{-2}], g_u is the statistical weight of the upper state of each level, $Q_{T_{rot}}$ is the rotational partition function evaluated at a rotational temperature T_{rot}, A_{ul} is the Einstein coefficient [s^{-1}], E_u/k is the energy of the upper level of the transition [K], ν_{ul} is the frequency of the $u \rightarrow l$ transition [s^{-1}], $\int T_{MB} dv$ is the velocity-integrated line intensity corrected from beam efficiency [K km s^{-1}], and η_{bf} is the beam filling factor. Assuming that the emission source has a 2D Gaussian shape, η_{bf} is equal to $\eta_{bf} = \theta_S^2 / (\theta_S^2 + \theta_B^2)$, with θ_B the HPBW of the telescope [arcsec] and θ_S the diameter of the Gaussian source [arcsec]. The values for ν_{ul}, E_u/k, g_u, and A_{ul} are taken from the MADEX spectral catalogue.

Rotational diagrams were built considering two limiting cases: (i) that the detected HCOOH emission is extended, with $\eta_{bf} = 1$; and (ii) that the emission is semi-extended, with $\theta_S = 9''$ (Cuadrado et al. 2015). In a plot of $\ln(N_u/g_u)$ *versus* the energy

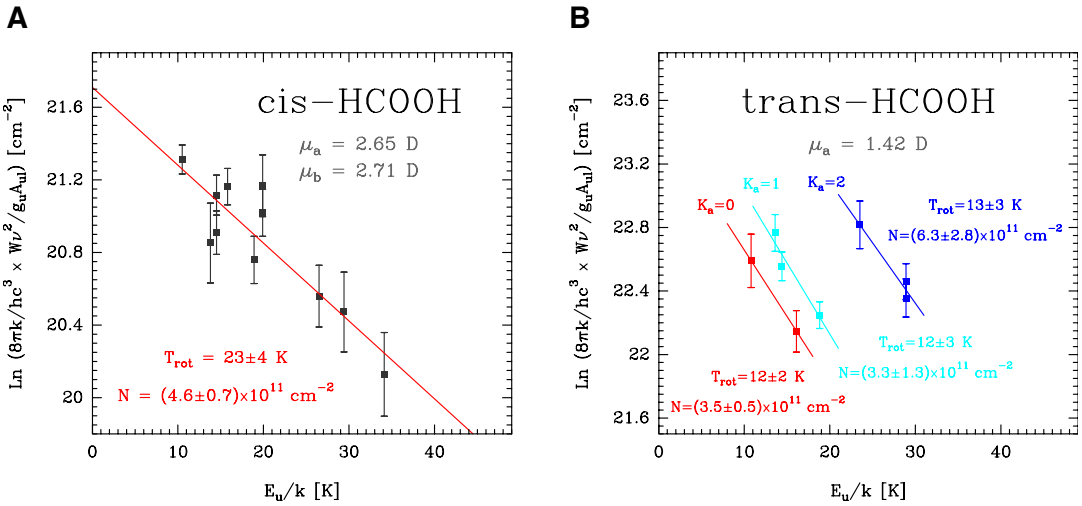

Fig. C.1. Rotational population diagrams from the observed HCOOH lines towards the Orion Bar, (+10″, -10″) position. *Left*: Diagram for the *cis* conformer (measurements lie along a single component). *Right*: Diagram for the *trans* conformer showing how different K_a rotational ladders split in different components. Fitted values of the rotational temperature, T_{rot}, and column density, N, are indicated in each panel (see also Table C.1).

Table C.1. Rotational temperatures (T_{rot}), column densities (N), and abundances towards the Orion Bar PDR, (+10″,-10″) position.

	Extended source		Semi-extended source			
	T_{rot} [K]	N(X) [cm^{-2}]	T_{rot} [K]	N(X) [cm^{-2}]	Abundance*	Notes
cis-HCOOH	23 (4)	4.6 (0.7) × 10^{11}	21 (4)	4.2 (0.6) × 10^{12}		a
trans-HCOOH K_a = 0	12 (2)	3.5 (0.5) × 10^{11}	6 (1)	4.1 (0.6) × 10^{12}		a, b
trans-HCOOH K_a = 1	12 (3)	3.3 (1.3) × 10^{11}	6 (1)	3.6 (2.1) × 10^{12}		a
trans-HCOOH K_a = 2	13 (3)	6.3 (2.8) × 10^{11}	7 (1)	5.0 (2.4) × 10^{12}		a
[(*cis*+*trans*)-HCOOH]	—	1.8 (0.3) × 10^{12}	—	1.7 (0.3) × 10^{13}	(0.3 − 2.7) × 10^{-10}	c

Notes. * The abundance of each species with respect to H nuclei is given by $\frac{N(X)}{N_H} = \frac{N(X)}{N(H)+2N(H_2)}$, with $N(H_2) \simeq 3 \times 10^{22}$ cm^{-2} and $N(H) \simeq 3 \times 10^{21}$ cm^{-2} (Cuadrado et al. 2015, and references therein). (a) Rotational temperatures and column densities from rotational diagram analysis. (b) ΔN calculated assuming an error of 15%. (c) Total column densities calculated as the sum of the *cis* and *trans* species.

of the upper level of each rotational transition, E_u/k, the population distribution roughly follows a straight line with a slope -1/T_{rot}. The total column density of the molecule, N, is obtained from the y-intercept and the partition function. Figure C.1 shows the resulting rotational diagrams assuming extended emission. Table C.1 lists the T_{rot} and N obtained by linear least squares fits. The uncertainties shown in Table C.1 indicate the uncertainty obtained in the fit. The uncertainties obtained in the determination of the fit line parameters with CLASS are included in the error bars at each point of the rotational diagram.

To crosscheck that the relative intensities of the detected *cis*- and *trans*-HCOOH rotational lines are those expected according to their inferred rotational temperatures (i.e. that the assigned lines are not blended with lines from other molecules), we carried out a simple excitation and radiative transfer calculation using MADEX. We assumed that the *cis*- and *trans*-HCOOH rotational levels are populated following a Boltzmann distribution at a single rotational temperature (obtained from the rotational diagrams). For a given column density N, the model computes each line opacity (optically thin for the observed HCOOH lines) assuming a Gaussian line profile (for a linewidth of 2 km s^{-1}) and simulates the output mm spectrum at a given spectral resolution. Figures 2 and D.1 show the observed spectra (black histograms) and the modelled lines (red curves) for the T_{rot} and N values obtained assuming extended emission. The good agreement of the fits, and lack of any other candidate line from a different molecule in our catalogue, confirms that all detected lines belong to *cis*- and *trans*-HCOOH.

Appendix E: Non-detection of *cis*-HCOOH towards the Orion BN/KL hot core and Barnard-B1

We searched for *cis*-HCOOH in regions shielded from strong FUV radiation fields. We selected chemically rich sources for which we have also carried out deep mm-line surveys with the IRAM-30m telescope. In particular, we searched for HCOOH towards the hot core in Orion BN/KL (Tercero et al. 2010) and towards the quiescent dark cloud Barnard 1-b (B1-b; Cernicharo et al. 2012). Although we clearly detected lines from *trans*-HCOOH towards both sources, we did not find lines from *cis*-HCOOH above the detection limit of these deep surveys. Using the MADEX excitation code, we derived lower limits to the *trans*-to-*cis* abundance ratio towards these sources. Below we summarise the main results from these observations:

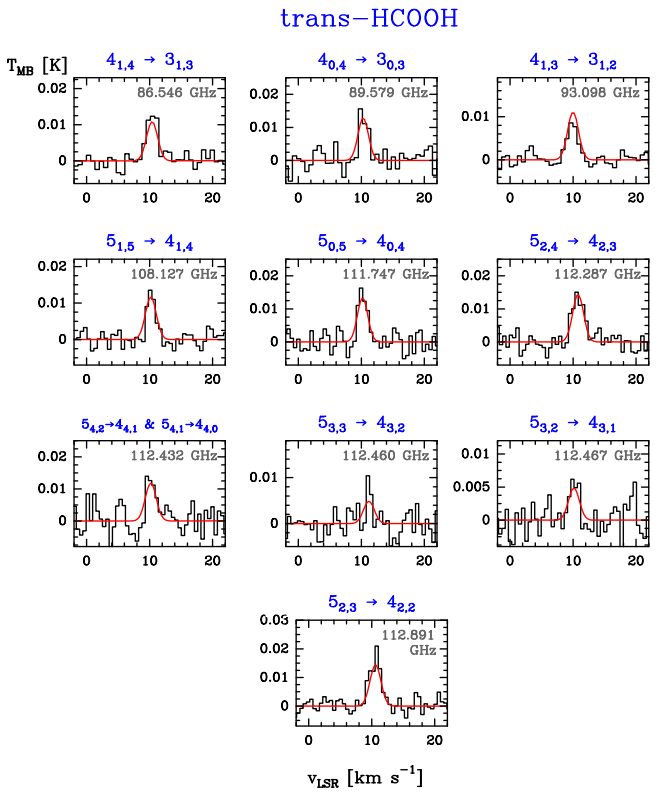

Fig. D.1. Detected *trans*-HCOOH rotational lines towards the edge of the Bar, (+10″, -10″) position. The ordinate refers to the intensity scale in main beam temperature units, and the abscissa to the LSR velocity. Line frequencies (in GHz) are indicated at the top-right of each panel together with the rotational quantum numbers (in blue). The red curve shows an excitation model that reproduces the observations. *Cis*-HCOOH lines are shown in Fig. 2.

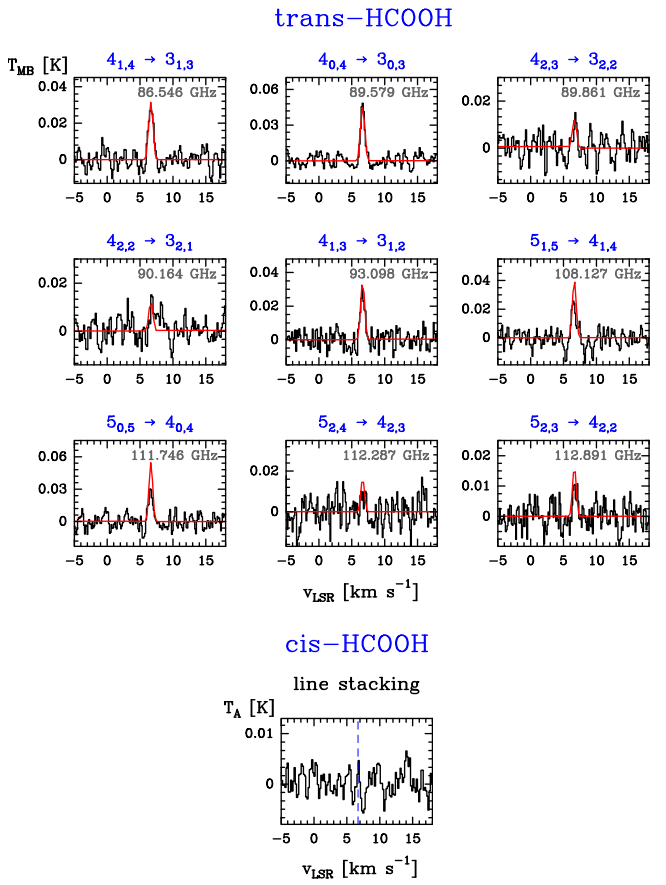

Fig. E.1. Detected *trans*-HCOOH rotational lines towards the cold cloud Barnard 1-b. The ordinate refers to the intensity scale in main beam temperature units and the abscissa to the Doppler velocity. Line frequencies (in GHz) are indicated at the top of each panel together with the rotational quantum numbers. The red curve shows an excitation model that reproduces the rotational population diagram. The bottom panel shows the stacked spectra for *cis*-HCOOH.

Orion BN/KL hot core: the hot core is embedded in the Becklin-Neugebauer/Kleinmann-Low massive star-forming region, at ∼4′ North-West from the Orion Bar, and ∼0.5′ North-West from the Trapezium stars. Relatively narrow lines ($\Delta v_{FWHM} \approx 3$ km s^{-1}) corresponding to *a*-type transitions of *trans*-HCOOH, with upper level energies up to $E_u/k \approx 300$ K, are detected at a LSR velocity of ∼8 km s^{-1}. The observed line parameters are consistent with emission from the hot core itself. This is dense, n_H of a few 10^7 cm^{-3}, and hot gas at about 200 K (Blake et al. 1987; Tercero et al. 2010), and also from the more extended warm gas (about 60 K) in the ambient molecular cloud, so-called the extended ridge (Blake et al. 1987; Tercero et al. 2010). Using MADEX and our accumulated knowledge of the source structure (see Tercero et al. 2010; Cernicharo et al. 2016 and references therein), we determine $T_{rot}(trans) = 100 \pm 35$ K and $N(trans) = (1.0 - 0.3) \times 10^{15}$ cm^{-2} in the hot core, and $T_{rot}(trans) = 40 \pm 15$ K and $N(trans) = (1.0 - 0.3) \times 10^{14}$ cm^{-2} in the extended ridge. We note that the extended ridge is the main responsible for the observed *trans*-HCOOH line emission in the 3 mm band. Although we obtain much higher *trans*-HCOOH column densities compared to the Orion Bar, lines from *cis*-HCOOH are not detected towards the hot core. Assuming $T_{rot}(trans) = T_{rot}(cis)$, we compute a lower limit to the *trans*-to-*cis* abundance ratio of >100 in the hot core, and >30 in the extended ridge.

B1-b cold cloud: Barnard 1 is a low mass star-forming region located in the Perseus cloud. The cold core B1-b harbours two submillimetre continuum sources (B1-bN and B1-bS) identified as first hydrostatic core candidates (Gerin et al. 2015), and B1b-W, an infrared source detected with Spitzer (Jørgensen et al. 2006). Complex organic molecules such as CH_3OCOH, CH_3SH, and CH_3O have been identified (Marcelino 2007; Öberg et al. 2010; Cernicharo et al. 2012). We detect nine lines from *trans*-HCOOH in the 3 mm band. A rotational diagram provides $T_{rot}(trans) = 12 \pm 4$ K and $N(trans) = (1.5 \pm 0.5) \times 10^{12}$ cm^{-2}. Figure E.1 shows the detected lines together with our best model fit (red curve). Lines are very narrow ($\Delta v_{FWHM} \approx 0.5$ km s^{-1}), consistent with emission from quiescent cold gas (about 20 K) shielded from FUV radiation. Although the inferred *trans*-HCOOH column density is similar to that obtained towards the Orion Bar, we do not detect lines from *cis*-HCOOH at the noise level of the B1-b data. Assuming $T_{rot}(trans) = T_{rot}(cis)$, we determine a lower limit to the *trans*-to-*cis* abundance ratio of >60. This is similar to that of the extended molecular Ridge of Orion, but significantly higher than towards the Bar.

Appendix F: Detected *cis*- and *trans*-HCOOH lines towards the Orion Bar PDR

Table F.1. Line parameters for *cis*-HCOOH towards the Orion Bar, (+10″, -10″) position.

Transition	Frequency	E_u	A_{ul}	S_{ij}	g_u	$\int T_{MB} dv$	v_{LSR}	Δv	T_{MB}	S/N
$(J_{K_a,K_c})_u \rightarrow (J_{K_a,K_c})_l$	[MHz]	[K]	[s^{-1}]			[mK km s^{-1}]	[km s^{-1}]	[km s^{-1}]	[mK]	
$4_{1,3} \rightarrow 4_{0,4}$	82740.491	14.5	2.32×10^{-5}	4.3	9	18.9(2.3)	10.5(0.2)	1.8(0.4)	8.7	4.7
$4_{1,4} \rightarrow 3_{1,3}$	85042.744	13.8	2.10×10^{-5}	3.7	9	15.3(3.5)	10.6(0.3)	2.1(0.5)	6.6	3.5
$5_{1,4} \rightarrow 5_{0,5}$	86556.490	19.9	2.59×10^{-5}	5.1	11	26.3(3.5)	10.0(0.2)	2.4(0.4)	10.1	5.6
$4_{0,4} \rightarrow 3_{0,3}$	87694.689	10.5	2.45×10^{-5}	4.0	9	26.6(2.3)	10.6(0.1)	2.0(0.2)	12.7	9.6
$4_{1,3} \rightarrow 3_{1,2}$	90661.090	14.5	2.54×10^{-5}	3.7	9	21.2(2.4)	10.3(0.1)	1.8(0.3)	11.2	4.8
$7_{0,7} \rightarrow 6_{1,6}$	90910.082	29.4	1.50×10^{-5}	3.5	15	10.9(2.4)	10.1(0.2)	1.5(0.4)	6.9	3.9
$6_{1,5} \rightarrow 6_{0,6}$	91291.549	26.5	2.95×10^{-5}	5.9	13	20.1(3.5)	10.3(0.2)	2.5(0.6)	7.5	5.7
$7_{1,6} \rightarrow 7_{0,7}$	97025.449	34.1	3.42×10^{-5}	6.6	15	15.5(2.4)	10.5(0.1)	1.8(0.3)	7.0	4.4
$8_{1,7} \rightarrow 8_{0,8}$	103845.157	42.8	4.02×10^{-5}	7.1	17	20.5(3.6)	10.0(0.2)	1.6(0.2)	12.2	5.2
$5_{1,5} \rightarrow 4_{1,4}$	106266.589	18.9	4.28×10^{-5}	4.8	11	22.2(2.4)	10.7(0.1)	1.8(0.3)	11.0	4.5
$5_{0,5} \rightarrow 4_{0,4}$	109470.705	15.8	4.87×10^{-5}	5.0	11	35.7(3.6)	10.3(0.1)	1.8(0.2)	18.6	7.1
$5_{1,4} \rightarrow 4_{1,3}$	113286.704	19.9	5.19×10^{-5}	4.8	11	39.6(5.3)	10.7(0.2)	1.9(0.3)	19.7	6.0

Table F.2. Line parameters for *trans*-HCOOH towards the Orion Bar, (+10″, -10″) position.

Transition	Frequency	E_u	A_{ul}	S_{ij}	g_u	$\int T_{MB} dv$	v_{LSR}	Δv	T_{MB}	S/N
$(J_{K_a,K_c})_u \rightarrow (J_{K_a,K_c})_l$	[MHz]	[K]	[s^{-1}]			[mK km s^{-1}]	[km s^{-1}]	[km s^{-1}]	[mK]	
$4_{1,4} \rightarrow 3_{1,3}$	86546.180	13.6	6.35×10^{-6}	3.7	9	23.8(3.5)	10.4(0.1)	1.8(0.3)	13.7	7.0
$4_{0,4} \rightarrow 3_{0,3}$	89579.168	10.8	7.51×10^{-6}	4.0	9	27.9(4.7)	10.3(0.1)	1.8(0.2)	14.9	5.3
$4_{2,3} \rightarrow 3_{2,2}$	89861.473	23.5	5.69×10^{-6}	3.0	9	26.4(7.0)	10.0(0.4)	2.2(0.7)	11.3	3.0
$4_{1,3} \rightarrow 3_{1,2}$	93098.350	14.4	7.91×10^{-6}	3.7	9	26.3(2.4)	10.0(0.1)	2.2(0.2)	9.9	6.2
$5_{1,5} \rightarrow 4_{1,4}$	108126.709	18.8	1.30×10^{-5}	4.8	11	28.7(2.4)	10.2(0.1)	1.5(0.2)	14.0	8.3
$5_{0,5} \rightarrow 4_{0,4}$	111746.771	16.1	1.49×10^{-5}	5.0	11	27.9(3.6)	10.2(0.1)	1.7(0.3)	16.2	5.2
$5_{2,4} \rightarrow 4_{2,3}$	112287.131	28.9	1.27×10^{-5}	4.2	11	32.2(3.6)	10.7(0.1)	2.1(0.2)	14.2	6.1
$5_{3,3} \rightarrow 4_{3,2}$	112459.608	44.8	9.73×10^{-6}	3.2	11	9.1(3.6)	11.2(0.1)	0.5(0.4)	16.5	5.2
$5_{3,2} \rightarrow 4_{3,1}$	112466.993	44.8	9.73×10^{-6}	3.2	11	14.0(3.6)	10.1(0.3)	1.8(0.5)	7.3	2.8
$5_{4,2} \rightarrow 4_{4,1}$	112432.278	67.1	5.47×10^{-6}	1.8	11	⟩ 24.9(6.1)	10.2(0.2)	1.6(0.4)	14.4	3.1
$5_{4,1} \rightarrow 4_{4,0}$	112432.305	67.1	5.47×10^{-6}	1.8	11					
$5_{2,3} \rightarrow 4_{2,2}$	112891.429	28.9	1.29×10^{-5}	4.2	11	29.2(3.6)	10.6(0.1)	2.0(0.2)	17.6	7.3